

1    **Rapid assessment of the mechanical response of deeply-buried tunnels:  
2    Governing equations, parameter calibration, and GUI design**

3                          **Zhihang Li** 

4    1. Department of Civil and Environmental Engineering, Monash University, VIC 3800, Australia  
5                          Email: zhihang.li@monash.edu

6                          **Qianbing Zhang** 

7    1. Department of Civil and Environmental Engineering, Monash University, VIC 3800, Australia  
8                          Email: Qianbing.Zhang@monash.edu

9                          **Chunshun Zhang** 

10    2. School of Civil Engineering, Wuhan University, Wuhan, Hubei 430072, China  
11                          Email: chunshun.zhang@whu.edu.cn

12                          **Luming Shen** 

13    3. School of Civil Engineering, the University of Sydney, NSW 2006, Australia  
14                          Email: luming.shen@sydney.edu.au

15                          **Yaolan Tang\*** 

16    3. School of Civil Engineering, the University of Sydney, NSW 2006, Australia

17                          \*Corresponding author, Email: yaolan.tang@sydney.edu.au

18                          **Jian Zhao** 

19    1. Department of Civil and Environmental Engineering, Monash University, VIC 3800, Australia  
20                          Email: jian.zhao@monash.edu

21    **Abstract**

22    A GUI-based framework is developed for the rapid assessment of deformation in deeply buried tunnels  
23    by integrating a nonlinear analytical rock (NAR) constitutive representation with a semi-analytical tunnel  
24    formulation. The framework incorporates automated procedures for determining constitutive parameters  
25    from triaxial laboratory tests and provides alternative parameter estimation routes based on commonly  
26    used empirical indices when test data are unavailable. These inputs are directly utilised in a semi-analytical  
27    calculation scheme to efficiently evaluate tunnel deformation and generate corresponding visual outputs. The  
28    proposed implementation facilitates a streamlined workflow from parameter input to deformation assessment,  
29    offering an efficient analysis option for preliminary tunnel design and engineering evaluation.

30    **Keywords:** Deeply buried tunnels; Semi-analytical method; Constitutive modelling; Parameter calibration;  
31    Graphical user interface (GUI).

32    **Highlights**

- 33    • A unified framework coupling a nonlinear analytical constitutive model with semi-analytical solutions  
34    for tunnel assessment.
- 35    • Automated calibration of constitutive parameters directly from lab data.
- 36    • Seamless integration of geological indices ( $GSI, D$ ) into constitutive inputs via built-in empirical in-  
37    terfaces.
- 38    • A comprehensive GUI facilitating an efficient workflow from constitutive response analysis to tunnel  
39    deformation visualization.

## 40 1. Introduction

41 With the rapid development of deep underground engineering, an increasing number of tunnels are being  
42 constructed at great depths (Mao et al., 2026; B. Wang et al., 2025; H. Wang et al., 2025; X. Wang et al.,  
43 2025). As excavation depth increases, tunnel excavation induces pronounced stress redistribution, causing  
44 the surrounding rock mass to experience a wide stress range, from high confinement in the far field to  
45 low or near-zero confinement at the tunnel wall. Under such conditions, tunnel stability and deformation  
46 behaviour are governed by the coupled effects of high in-situ stress, excavation-induced unloading, and com-  
47 plex geological environments (Qiao et al., 2023; Shi et al., 2026). Reliable assessment of tunnel deformation  
48 and stress redistribution is therefore essential for support design, construction safety, and long-term service  
49 performance in deep underground engineering projects.

50 Semi-analytical methods for evaluating deformation around deeply buried tunnels constitute a classical and  
51 practical approach in rock mechanics, offering high efficiency and clear physical interpretation for rapid  
52 assessment and preliminary design (Lu et al., 2026; Xiao et al., 2023, 2024). A fundamental prerequisite of  
53 such methods is an appropriate constitutive description of the surrounding rock mass. However, experimental  
54 observations indicate that rock behaviour is inherently complex, involving non-linear pre-peak hardening,  
55 post-peak softening (Cai et al., 2021; Hou & Cai, 2023), brittle–ductile transition (Li et al., 2025; Shen,  
56 2024), and contraction–dilation behaviour (Meng et al., 2025; Xing et al., 2024), which requires constitutive  
57 models capable of representing these features in a comprehensive and consistent manner.

58 Beyond model formulation, practical application also requires that constitutive parameters be determined  
59 in a reliable and efficient manner. Parameters lacking clear physical meaning or requiring extensive manual  
60 tuning can significantly limit the applicability of constitutive models in engineering analysis. Consequently,  
61 automated or systematic calibration procedures based on experimental data are highly desirable (Honório  
62 et al., 2024). Furthermore, many existing rock constitutive models are primarily developed from laboratory  
63 test results, with limited consideration of their transferability to field conditions, where material properties  
64 are often characterised using empirical indices rather than detailed experimental data (Aydan et al., 1997;  
65 Chen et al., 2025). At the same time, despite substantial theoretical developments, most semi-analytical ap-  
66 proaches are implemented as internal research codes, and software-level tools suitable for routine engineering  
67 practice remain scarce.

68 To address the above challenges, this study presents an integrated framework that builds upon and extends  
69 our previously proposed non-linear analytical rock (NAR) constitutive model (Tang et al., 2025) and its  
70 associated semi-analytical solution for deeply buried tunnels. The framework incorporates an automated  
71 calibration procedure that enables constitutive parameters to be efficiently identified directly from exper-  
72 imental test data. In situations where laboratory data are limited or unavailable, a systematic interface  
73 is further developed to link the constitutive parameters with commonly used empirical methods and field-  
74 based indices. Based on these developments, a fast and consistent semi-analytical scheme is established for  
75 evaluating tunnel deformation under deep-buried conditions. Together, these components are implemented  
76 in a dedicated and user-friendly graphical user interface (GUI), providing a practical and efficient tool for  
77 rapid assessment and preliminary design in deep underground engineering.

78 The paper is structured as follows. Section 2 briefly reviews the NAR model. Section 3 presents the  
79 semi-analytical formulation for evaluating deformation around deeply buried tunnels based on the NAR  
80 model. Section 4 introduces the automated parameter calibration procedure and the empirical parameter  
81 transformation framework. Section 5 describes the development and implementation of the graphical user  
82 interface and demonstrates its application through representative examples. Finally, Section 6 summarises

83 the main findings and conclusions of this study.

## 84 2. Non-linear analytical constitutive model for rocks

85 This section presents the non-linear analytical constitutive model for rocks (NAR model) proposed by Tang  
86 et al. (2025). The pressure-dependent characteristics of the peak and residual states are first defined, followed  
87 by the formulation of continuous strength evolution and lateral deformation laws. These closed-form expres-  
88 sions constitute the theoretical basis for the subsequent semi-analytical solution and GUI implementation  
89 for deeply-buried tunnels.

### 90 2.1. Pressure-dependent peak and residual states

91 The key states of the constitutive response, namely the peak and residual points, are formulated as functions  
92 of the confining pressure  $\sigma_3$ . The peak maximum principal stress  $\sigma_1^p$  is expressed as

$$\sigma_1^p(\sigma_3) = \sigma_3 + (A^p\sigma_3 + B^p)^{C^p}, \quad (1)$$

93 where  $A^p$ ,  $B^p$ , and  $C^p$  are material parameters. The residual strength  $\sigma_1^r$  follows an analogous form,

$$\sigma_1^r(\sigma_3) = \sigma_3 + (A^r\sigma_3 + B^r)^{C^r}, \quad (2)$$

94 with  $A^r$ ,  $B^r$ , and  $C^r$  denoting the corresponding residual-state parameters. The peak axial strain  $\varepsilon_1^p$ , which  
95 generally exhibits a non-linear dependence on  $\sigma_3$ , is described by a power-law relationship,

$$\varepsilon_1^p(\sigma_3) = A^e\sigma_3^{B^e} + C^e, \quad (3)$$

96 where  $A^e$ ,  $B^e$ , and  $C^e$  govern the pressure-dependency of the peak strain evolution.

### 97 2.2. Strength evolution and lateral deformation laws

98 Following the analytical framework proposed by Tang et al. (2025), the full-range stress-strain response is  
99 governed by two coupled evolution functions. The strength evolution function  $f$  describes the transition  
100 from pre-peak hardening to post-peak softening:

$$f(\sigma_1, \varepsilon_1, \sigma_3) = \begin{cases} \sigma_1 - (\sigma_1^p - \sigma_3) \frac{n_h \gamma}{n_h - 1 + \gamma^{n_h}} - \sigma_3, & 0 \leq \gamma < 1, \\ \sigma_1 - (\sigma_1^p - \sigma_1^r) \frac{n_s \gamma}{n_s - 1 + \gamma^{n_s}} - \sigma_1^r, & \gamma \geq 1, \end{cases} \quad (4)$$

101 where  $\gamma = \varepsilon_1 / \varepsilon_1^p$  is the normalized axial strain, and  $n_h$  and  $n_s$  are dimensionless shape parameters controlling  
102 the curvature of the hardening and softening branches, respectively.

103 The lateral deformation function  $g$  governs the evolution of volumetric deformation, including dilatancy  
104 effects:

$$g(\varepsilon_3, \varepsilon_1, \sigma_3) = \begin{cases} \varepsilon_3 + \frac{\mu \varepsilon_1^{\beta_h+1}}{(\varepsilon_1^p)^{\beta_h}}, & 0 \leq \gamma < 1, \\ \varepsilon_3 + \mu \varepsilon_1^p + 0.5(\varepsilon_1 - \varepsilon_1^p) + (\mu \beta_h + \mu - 0.5) \frac{(\varepsilon_1^p)^{\beta_s} [\varepsilon_1^{1-\beta_s} - (\varepsilon_1^p)^{1-\beta_s}]}{1 - \beta_s}, & \gamma \geq 1, \end{cases} \quad (5)$$

105 where  $\mu = -\varepsilon_3^p/\varepsilon_1^p$  quantifies the lateral expansion intensity at peak stress, and  $\beta_h$  and  $\beta_s$  are shape  
 106 parameters governing lateral strain evolution in the pre-peak and post-peak regimes, respectively.  
 107 For numerical implementation within the GUI framework, the equilibrium state at each loading increment  
 108 is obtained by enforcing

$$f(\sigma_1, \varepsilon_1, \sigma_3) = 0, \quad g(\varepsilon_3, \varepsilon_1, \sigma_3) = 0. \quad (6)$$

109 This dual-constraint formulation ensures that the computed stress-strain trajectory simultaneously satisfies  
 110 strength evolution and deformation compatibility throughout the entire loading process. To quantify the  
 111 stiffness-reduction during loading process, a index  $R$  is introduced, which governs the progressive degradation  
 112 of stiffness during unloading and reloading paths:

$$R = \begin{cases} 0, & \varepsilon_1 < \varepsilon_1^p, \\ \frac{\sigma_1^p - \sigma_1}{\sigma_1^p - \sigma_1^r}, & \varepsilon_1 \geq \varepsilon_1^p. \end{cases} \quad (7)$$

### 113 3. Semi-analytical solution for deeply-buried tunnels

114 A semi-analytical framework is developed to determine the mechanical response of deeply-buried circular  
 115 tunnels under hydrostatic loading. The governing constitutive behavior for the rock mass, characterized  
 116 by the strength evolution function  $f$  and lateral deformation function  $g$ , is implemented according to the  
 117 theoretical formulations in Sec. 2.2. Specifically, the tangential stress  $\sigma_\theta$  is determined by the equilibrium  
 118 condition  $f(\sigma_\theta, \varepsilon_\theta, \sigma_r) = 0$ :

$$f(\sigma_\theta, \varepsilon_\theta, \sigma_r) = \begin{cases} \sigma_\theta - (\sigma_\theta^p - \sigma_r) \frac{n_h \gamma}{n_h - 1 + \gamma^{n_h}} - \sigma_r, & 0 \leq \gamma < 1, \\ \sigma_\theta - (\sigma_\theta^p - \sigma_\theta^r) \frac{n_s \gamma}{n_s - 1 + \gamma^{n_s}} - \sigma_\theta^r, & \gamma \geq 1. \end{cases} \quad (8)$$

119 The radial strain  $\varepsilon_r$  is subsequently obtained through the compatibility constraint  $g(\varepsilon_r, \varepsilon_\theta, \sigma_r) = 0$ :

$$g(\varepsilon_r, \varepsilon_\theta, \sigma_r) = \begin{cases} \varepsilon_r + \frac{\mu (\varepsilon_\theta)^{\beta_h+1}}{(\varepsilon_\theta^p)^{\beta_h}}, & 0 \leq \gamma < 1, \\ \varepsilon_r + \mu \varepsilon_\theta^p + 0.5(\varepsilon_\theta - \varepsilon_\theta^p) + (\mu \beta_h + \mu - 0.5) \frac{(\varepsilon_\theta^p)^{\beta_s} [(\varepsilon_\theta)^{1-\beta_s} - (\varepsilon_\theta^p)^{1-\beta_s}]}{1 - \beta_s}, & \gamma \geq 1. \end{cases} \quad (9)$$

120 To derive the solution, the radial domain is discretized into  $N$  concentric rings, as shown in Fig. 1. The  
 121 radial stress distribution is defined incrementally from the far-field boundary to the tunnel wall:

$$\sigma_{r(i)} = p_0 + i \Delta \sigma_r, \quad \Delta \sigma_r = \frac{p_u - p_0}{N}, \quad (i = 0, 1, \dots, N), \quad (10)$$

122 where  $p_0$  and  $p_u$  denote the initial in-situ pressure and the internal support pressure, respectively. At  
 123 the far-field boundary ( $i = 0$ ), the stress state satisfies the hydrostatic condition  $\sigma_{r(0)} = \sigma_{\theta(0)} = p_0$ . Under  
 124 axisymmetric plane-strain conditions, the strain compatibility and stress equilibrium equations are expressed  
 125 as:

$$\begin{cases} \frac{\varepsilon_\theta - \varepsilon_r}{r} + \frac{d\varepsilon_\theta}{dr} = 0, \\ \frac{\sigma_r - \sigma_\theta}{r} + \frac{d\sigma_r}{dr} = 0. \end{cases} \quad (11)$$

126 By eliminating the radial coordinate  $r$  from Eq. (11), the following relation is obtained:

$$\frac{\varepsilon_\theta - \varepsilon_r}{d\varepsilon_\theta} = \frac{\sigma_r - \sigma_\theta}{d\sigma_r} = -\frac{r}{dr}. \quad (12)$$

127 Following the iterative procedure proposed by Tang et al. (2025), the tangential strain at the  $i$ -th ring is  
128 updated from the state of the preceding ring using a forward-difference scheme:

$$\varepsilon_{\theta(i)} = \varepsilon_{\theta(i-1)} + \frac{\varepsilon_{\theta(i-1)} - \varepsilon_{r(i-1)}}{\sigma_{r(i-1)} - \sigma_{\theta(i-1)}} \Delta\sigma_r. \quad (13)$$

129 The corresponding  $\sigma_{\theta(i)}$  and  $\varepsilon_{r(i)}$  values are subsequently obtained by satisfying the constitutive constraints  
130  $f = 0$  and  $g = 0$ . Furthermore, the radius ratio between two adjacent rings,  $\zeta_{(i)}$ , is derived as:

$$\zeta_{(i)} = \frac{(\sigma_{r(i)} + \sigma_{r(i-1)}) - (\sigma_{\theta(i)} + \sigma_{\theta(i-1)}) + \Delta\sigma_r}{(\sigma_{r(i)} + \sigma_{r(i-1)}) - (\sigma_{\theta(i)} + \sigma_{\theta(i-1)}) - \Delta\sigma_r}. \quad (14)$$

131 The radius  $r_{(k)}$  and the radial displacement  $u_{r(k)}$  at any node  $k$  are thus determined by the following recursive  
132 relations:

$$r_{(k)} = R_0 \prod_{i=k+1}^N \zeta_i, \quad \text{and} \quad u_{r(k)} = \varepsilon_{\theta(k)} r_{(k)}, \quad (15)$$

133 where  $R_0$  (or  $r_{(N)}$ ) denotes the target radius of the tunnel excavation.

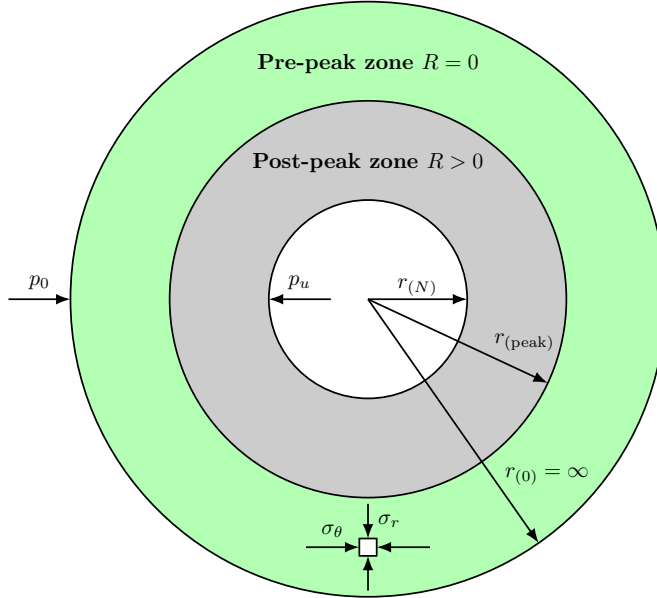


Figure 1. Calculation diagram and simulated results of deeply buried circular tunnels.

#### 134 4. Model parameters

##### 135 4.1. Automated calibration from triaxial experimental data

136 This section outlines the procedure for extracting key points from experimental stress-strain curves and  
137 performing automated parameter calibration. The analytical nature of the proposed model, integrated into  
138 the developed GUI, enables a streamlined, automated calibration workflow based on definitive geometric  
139 landmarks of the stress-strain response.

140 *Step I: Peak Strength and Strain*

141 The first step involves identifying the peak states on the axial stress-strain ( $\varepsilon_1-\sigma_1$ ) curves under different  
142 confining pressures  $\sigma_3$ . Two datasets are automatically extracted, namely  $(\sigma_3, \sigma_1^p)$  and  $(\sigma_3, \varepsilon_1^p)$ . These  
143 peak values are then used to perform nonlinear regression to determine the peak strength and peak strain  
144 envelopes, expressed as  $\sigma_1^p(\sigma_3) = \sigma_3 + (A^p\sigma_3 + B^p)^{C^p}$  and  $\varepsilon_1^p(\sigma_3) = A^e\sigma_3^{B^e} + C^e$ , respectively.

145 *Step II: Residual Strength*

146 In Step II, the residual strength  $\sigma_1^r$  is identified for each confining pressure as either the post-peak stress  
147 plateau or the minimum stress attained for  $\varepsilon_1 > \varepsilon_1^p$ . The extracted dataset  $(\sigma_3, \sigma_1^r)$  is subsequently fitted  
148 using the residual strength function  $\sigma_1^r(\sigma_3) = \sigma_3 + (A^r\sigma_3 + B^r)^{C^r}$ , thereby defining the residual strength  
149 envelope.

150 *Step III: Lateral Deformation Parameters*

151 The lateral deformation characteristics are determined in Step III. The peak axial and lateral strain pairs  
152  $(\varepsilon_1^p, \varepsilon_3^p)$  are extracted at the onset of post-peak deformation, from which the lateral expansion parameter  $\mu$   
153 is evaluated. Its dependence on confining pressure is then quantified through linear regression in the form  
154  $\mu(\sigma_3) = A_\mu\sigma_3 + B_\mu$ .

155 *Step IV: Physics-informed Curve-shaping*

156 Step IV constitutes an iterative, physics-informed calibration stage aimed at determining the curve-shaping  
157 parameters. Prior to optimisation, the experimental axial and lateral deformation data are normalised to  
158 ensure numerical stability and balanced contributions of different response components. The dimensionless  
159 parameters  $n_h$  and  $n_s$ , governing the curvature of the pre-peak hardening and post-peak softening branches,  
160 together with the lateral deformation parameters  $\beta_h$  and  $\beta_s$ , are treated as a coupled parameter set. An  
161 iterative optimisation procedure is then carried out by minimising a unified objective function that measures  
162 the discrepancy between model-predicted and experimental axial stress and lateral strain responses. The  
163 parameters  $\{n_h, n_s, \beta_h, \beta_s\}$  are updated jointly within this loop until the convergence criterion is satisfied,  
164 after which the calibrated parameter set is returned. The complete workflow of the automated constitutive  
165 parameter calibration is summarised in Fig. 2.

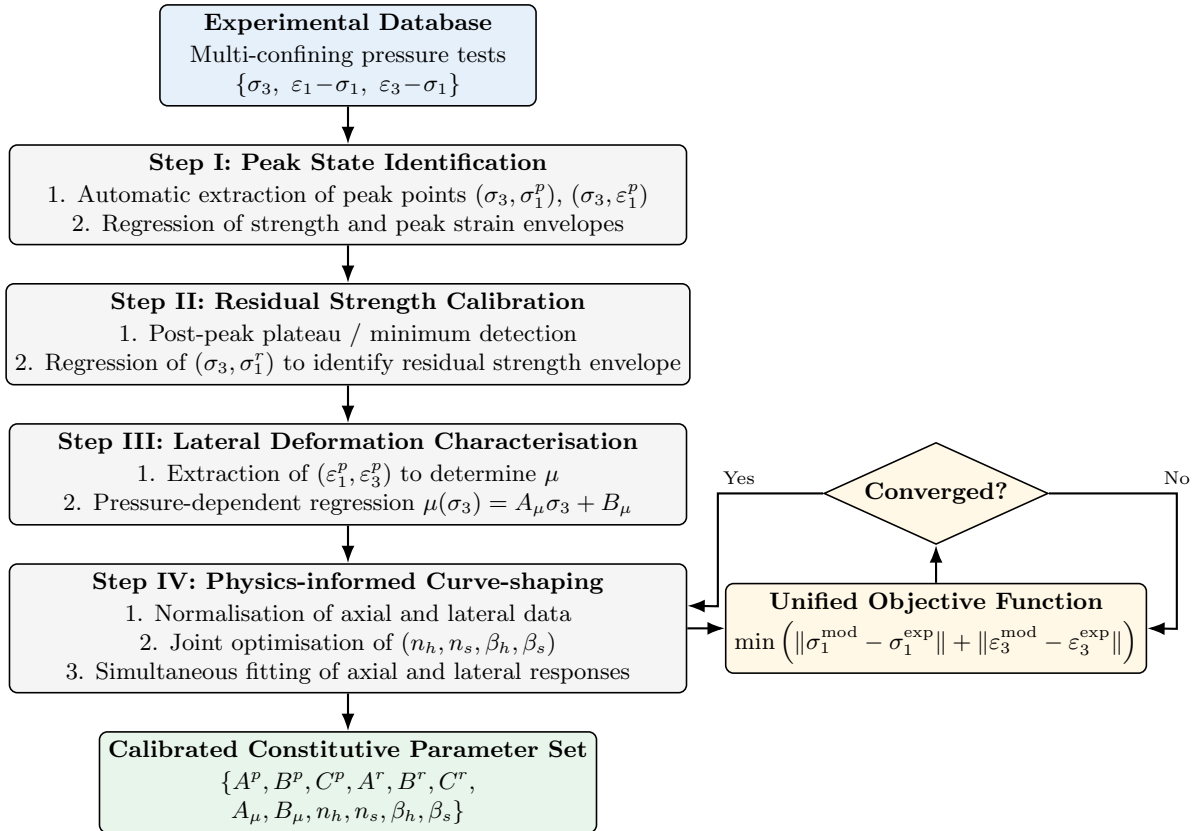


Figure 2. Flowchart of the fully automated, physics-informed calibration procedure for constitutive model parameters based on multi-confining pressure experimental data.

#### 166 4.2. Parameter estimation via empirical methods

167 In engineering practice, comprehensive triaxial test data may not always be available. To ensure the model's  
 168 applicability to field-scale problems, the GUI incorporates an empirical estimation module based on the  
 169 generalized Hoek-Brown (H-B) criterion. This interface allows the constitutive parameters to be derived from  
 170 widely-accepted rock mass classification indices, such as the Geological Strength Index (*GSI*), effectively  
 171 bridging the gap between theoretical modeling and practical site characterization.

##### 172 4.2.1. Peak and residual strength

173 The peak strength of the rock mass under an effective confining pressure  $\sigma_3$  is evaluated using the 2002  
 174 edition of the generalized Hoek–Brown criterion (Hoek et al., 2002):

$$\sigma_1^p = \sigma_3 + \sigma_{ci} \left( m_b \frac{\sigma_3}{\sigma_{ci}} + s \right)^a, \quad (16)$$

175 where  $\sigma_{ci}$  denotes the uniaxial compressive strength (UCS) of the intact rock. The rock mass parameters  
 176 ( $m_b$ ,  $s$ , and  $a$ ) are functions of the Geological Strength Index (*GSI*), the intact rock constant  $m_i$ , and the  
 177 disturbance factor  $D$ , expressed as

$$m_b = m_i \exp \left( \frac{GSI - 100}{28 - 14D} \right), \quad s = \exp \left( \frac{GSI - 100}{9 - 3D} \right), \quad a = \frac{1}{2} + \frac{1}{6} \left( e^{-GSI/15} - e^{-20/3} \right). \quad (17)$$

178 For post-peak behaviour, the residual strength of the rock mass is described by preserving the functional  
 179 form of the generalized Hoek–Brown criterion while introducing a residual geological index  $GSI_r$ . The

180 residual maximum principal stress  $\sigma_1^r$  is given by

$$\sigma_1^r = \sigma_3 + \sigma_{ci} \left( m_{br} \frac{\sigma_3}{\sigma_{ci}} + s_r \right)^{a_r}, \quad (18)$$

181 where the residual parameters  $m_{br}$ ,  $s_r$ , and  $a_r$  are obtained by replacing  $GSI$  with  $GSI_r$  in Eq. (17). The GUI  
182 allows either direct input of  $GSI_r$  or the use of a suggested empirical relation,  $GSI_r = GSI \exp(-0.134 GSI)$ ,  
183 proposed by Cai et al. (2007).

184 For numerical implementation and subsequent constitutive formulation, the Hoek–Brown parameters are  
185 recast into an equivalent analytical form as

$$\begin{aligned} A^p &= \frac{m_b}{\sigma_{ci}^{1-1/a}}, & B^p &= s \sigma_{ci}^{1/a}, & C^p &= a, \\ A^r &= \frac{m_{br}}{\sigma_{ci}^{1-1/a_r}}, & B^r &= s_r \sigma_{ci}^{1/a_r}, & C^r &= a_r. \end{aligned} \quad (19)$$

186 To incorporate strain-rate effects under dynamic loading conditions, a dynamic increase factor (DIF) is  
187 introduced by scaling the intact rock strength. The dynamic intact strength is defined as

$$\sigma_{ci}^{dyn} = \text{DIF } \sigma_{ci}, \quad (20)$$

188 while the original functional form of the Hoek–Brown criterion is retained. Accordingly, the dynamic peak  
189 strength is expressed as

$$\sigma_1^{p,dyn} = \sigma_3 + \sigma_{ci}^{dyn} \left( m_b \frac{\sigma_3}{\sigma_{ci}^{dyn}} + s \right)^a. \quad (21)$$

190 This formulation introduces strain-rate dependency through a physically meaningful scaling of the intrinsic  
191 material strength, without altering the nonlinear confinement dependency governed by the Hoek–Brown  
192 parameters.

193 Based on a comprehensive compilation of dynamic test data for a wide range of rock types, the strain-  
194 rate-dependent DIF is described using a piecewise empirical formulation, reflecting two distinct strain-rate  
195 regimes associated with different dominant failure mechanisms (Liu et al., 2018):

$$\text{DIF}(\dot{\varepsilon}) = \begin{cases} 1 + 0.15 \dot{\varepsilon}^{0.30}, & 10^{-6} \leq \dot{\varepsilon} \leq 10 \text{ s}^{-1}, \\ 1 + 0.10 \dot{\varepsilon}^{0.50}, & 10 < \dot{\varepsilon} \leq 10^4 \text{ s}^{-1}. \end{cases} \quad (22)$$

#### 196 4.2.2. Peak axial strain

197 The rock mass deformation modulus  $E_{rm}$  is estimated using two empirical scenarios proposed by Hoek &  
198 Diederichs (2006). When the intact rock modulus  $E_i$  is known,  $E_{rm}$  takes the following form:

$$E_{rm} = E_i \left\{ 0.02 + \frac{1 - D/2}{1 + \exp[(60 + 15D - GSI)/11]} \right\} \quad (23)$$

199 When  $E_i$  is unknown,  $E_{rm}$  is estimated directly as:

$$E_{rm} = 10^5 \left\{ \frac{1 - D/2}{1 + \exp[(75 + 25D - GSI)/11]} \right\} \quad (24)$$

200 Then, the axial strain at peak strength  $\varepsilon_{1p}$  is estimated as:

$$\varepsilon_1^p = \frac{\sigma_1^p}{E_{rm}}. \quad (25)$$

201 To establish an explicit analytical relationship between peak axial strain and confining pressure, a series  
202 of discrete data points  $(\sigma_3, \varepsilon_1^p)$  are first generated by combining the empirical estimation of  $E_{rm}$  with the  
203 corresponding peak strength  $\sigma_1^p(\sigma_3)$ . These generated data points serve as reference values representing the  
204 confinement-dependent peak deformation characteristics of the rock mass. The resulting dataset is then  
205 fitted using the following power-law function in Eq. (3). This formulation provides a smooth, closed-form  
206 description of the peak axial strain over a wide range of confining pressures, which is subsequently employed  
207 in the constitutive response and tunnel analysis modules.

#### 208 4.2.3. Rock mass Poisson's ratio

209 To account for the enhanced lateral deformability induced by rock mass discontinuities, the Poisson's ratio  
210  $\nu$  (approximated as  $\mu$  within the current numerical framework) is estimated as a function of the uniaxial  
211 compressive strength  $\sigma_c = \sigma_{ci} s^a$ . Following the empirical relationship established by Aydan et al. (1993),  
212 the parameter is defined by the following function:

$$\nu = \mu = 0.25 \left( 1 + e^{-0.2\sigma_c} \right). \quad (26)$$

213 This formulation effectively captures the inverse relationship between rock strength and lateral expansion,  
214 providing a reliable estimation for the equivalent continuum properties of jointed rock masses.

#### 215 4.2.4. User-defined parameters

216 While the aforementioned empirical relations provide robust estimates for primary geomechanical proper-  
217 ties, certain constitutive parameters governing the specific shape of the stress-strain curve, namely the  
218 hardening/softening indices  $(n_h, n_s)$  and the corresponding lateral deformation factors  $(\beta_h, \beta_s)$ , do not have  
219 widely established empirical correlations for direct prediction. Consequently, these parameters are left for  
220 the user to calibrate manually based on specific lithological data or project-specific requirements.

## 221 5. GUI design and implementation

222 To bridge the epistemological gap between the complex theoretical derivations presented in the preceding  
223 sections and their practical application in geotechnical engineering, a dedicated graphical user interface  
224 (GUI) platform, named *Tunnel Solver*, was developed within the Python ecosystem. This software represents  
225 a synergistic integration of the proposed strain-softening constitutive model and a high-performance semi-  
226 analytical solver. The primary objective of this development is to democratize advanced rock mechanics  
227 analysis. By encapsulating rigorous mathematical algorithms within an intuitive visual environment, the  
228 software provides engineers with a streamlined, robust tool for constitutive parameter calibration, empirical  
229 property estimation, and the rapid, quantitative assessment of tunnel convergence and plastic zone evolution  
230 under deep-buried conditions.

231 **5.1. System architecture and integrated workflow**

232 The software architecture is predicated on a modular design philosophy, strictly adhering to the Model-  
233 View-Controller (MVC) design pattern. This architectural paradigm ensures a clean separation of concerns,  
234 decoupling the internal computational logic (Model) from the user interaction layer (View) and the event  
235 handling mechanisms (Controller). This separation not only enhances software robustness but also facil-  
236 itates future scalability for integrating more complex constitutive laws. The system is composed of three  
237 distinct, yet interconnected functional layers:

238 **I. Model Layer (The Computational Kernel)**

239 Acting as the mathematical backbone of the system, this layer encapsulates the core analytical derivations  
240 and numerical algorithms. It is built upon the `NumPy` and `SciPy` scientific computing stacks to leverage  
241 vectorization for high-performance matrix operations. Specifically, it integrates two primary engines: the  
242 *Calibration Engine*, which employs a constrained Levenberg-Marquardt optimization algorithm for robust  
243 parameter inversion; and the *Simulation Engine*, which implements the finite difference discretization scheme  
244 described in Section 3 as an independent "black box," enabling rigorous unit testing.

245 **II. View Layer (The Visualization Interface)**

246 The presentation layer is responsible for all user interactions and real-time graphical rendering. Constructed  
247 using the `Tkinter` framework for its lightweight footprint and native OS integration, it avoids the latency of  
248 heavier web-based frameworks. For advanced scientific visualization, the `Matplotlib` library is seamlessly  
249 embedded via the `FigureCanvasTkAgg` backend, supporting interactive features such as zooming and real-  
250 time cursor tracking to generate publication-quality dual-axis plots.

251 **III. Controller Layer (The Logic Coordinator)**

252 The central controller class orchestrates the application lifecycle. A critical innovation here is the implemen-  
253 tation of a Global Shared Memory (State Persistence) mechanism. As illustrated in Fig. 3, this repository  
254 acts as a central data hub, ensuring seamless synchronization across modules. Constitutive parameters  
255 derived in the pre-processing modules are serialized into this shared memory and automatically retrieved  
256 when initializing the simulation kernel, thereby eliminating manual transcription errors and ensuring work-  
257 flow continuity.

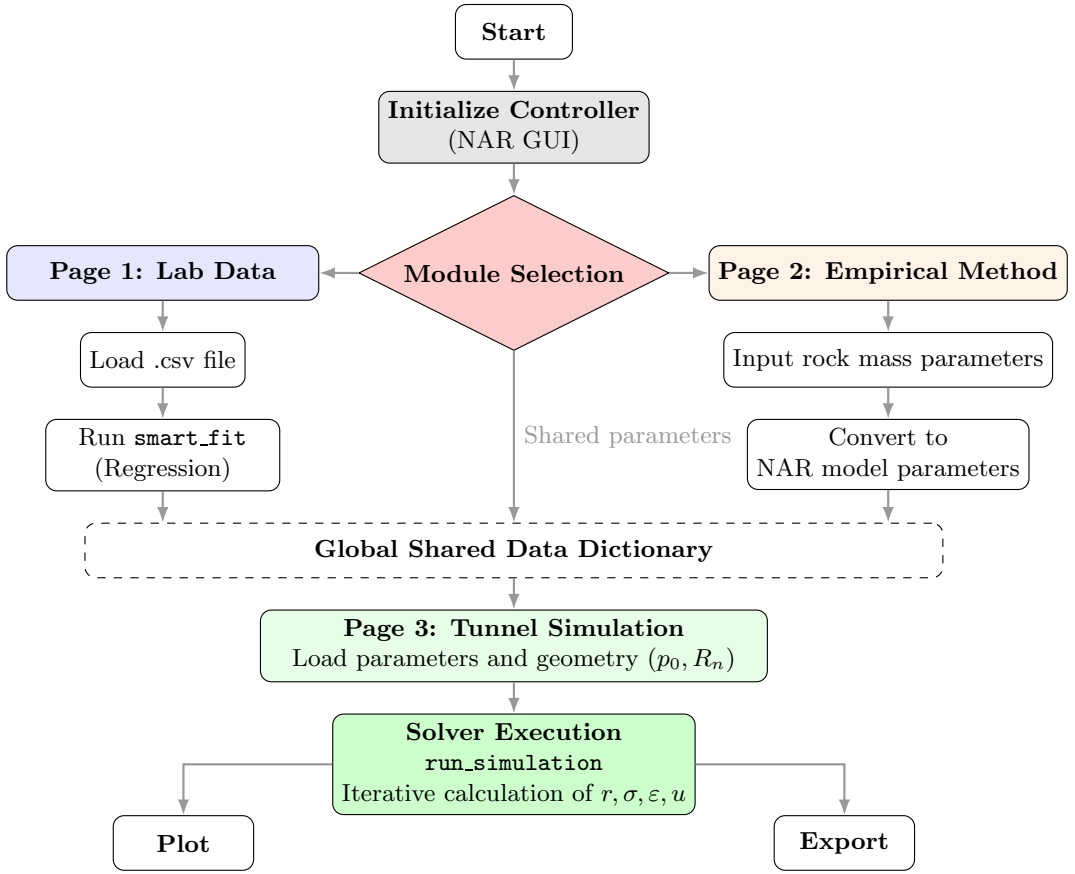


**Figure 3.** The architectural flowchart of *Tunnel Solver*, illustrating the MVC pattern and the strictly coupled data interaction between the calibration (Module 1), empirical estimation (Module 2), and tunnel simulation kernels (Module 3).

## 258 5.2. Functional modules and algorithmic implementation

259 The practical utility of the *Tunnel Solver* platform is realized through two specialized functional kernels:  
260 the *Material Characterization Kernel* (Modules 1 and 2) and the *Tunnel Simulation Kernel* (Module 3).  
261 This section details the algorithmic implementation and interaction logic of these kernels, illustrating the  
262 workflow from data ingestion to verified constitutive mapping and final engineering simulation.

### 263 Part A: Material characterization and constitutive mapping

264 Accurate determination of constitutive parameters is a prerequisite for reliable tunnel stability assessment.  
265 To accommodate the variability of data availability in engineering practice, the platform adopts a dual-  
266 pathway strategy, utilizing specific verification mechanisms to ensure numerical consistency.

267 **Module 1: Experimental-data-driven calibration** For advanced design stages utilizing laboratory  
268 triaxial data, Module 1 implements a rigorous calibration workflow. As illustrated in Fig. 4, the process  
269 integrates data management, algorithmic inversion, and visual verification into a coherent system.  
270 The workflow operates on a strict logic flow. First, the *Intelligent Data Ingestion* interface (Fig. 4a)  
271 parses raw experimental datasets, automatically grouping them by confining pressure and applying zero-  
272 offset corrections to ensure the physical validity of the stress-strain origin. Subsequently, the core "Smart  
273 Fit" engine executes a constrained nonlinear least-squares optimization. Upon convergence, the calibrated  
274 parameters are explicitly rendered in the *Parameter Output Panel* (Fig. 4b). This component serves as

275 a Quantitative Audit mechanism, allowing engineers to inspect specific coefficients (e.g.,  $A_p$ ,  $B_p$ ) before  
 276 acceptance.  
 277 To finally validate the inversion quality, the module features a real-time *Visualization Canvas* (Fig. 4c).  
 278 By superimposing the theoretical curves derived from the calibrated parameters onto the raw experimental  
 279 scatter points, engineers can qualitatively assess the goodness-of-fit, ensuring the model accurately captures  
 280 the pre- and post-peak characteristics.

## Calibration with lab tests

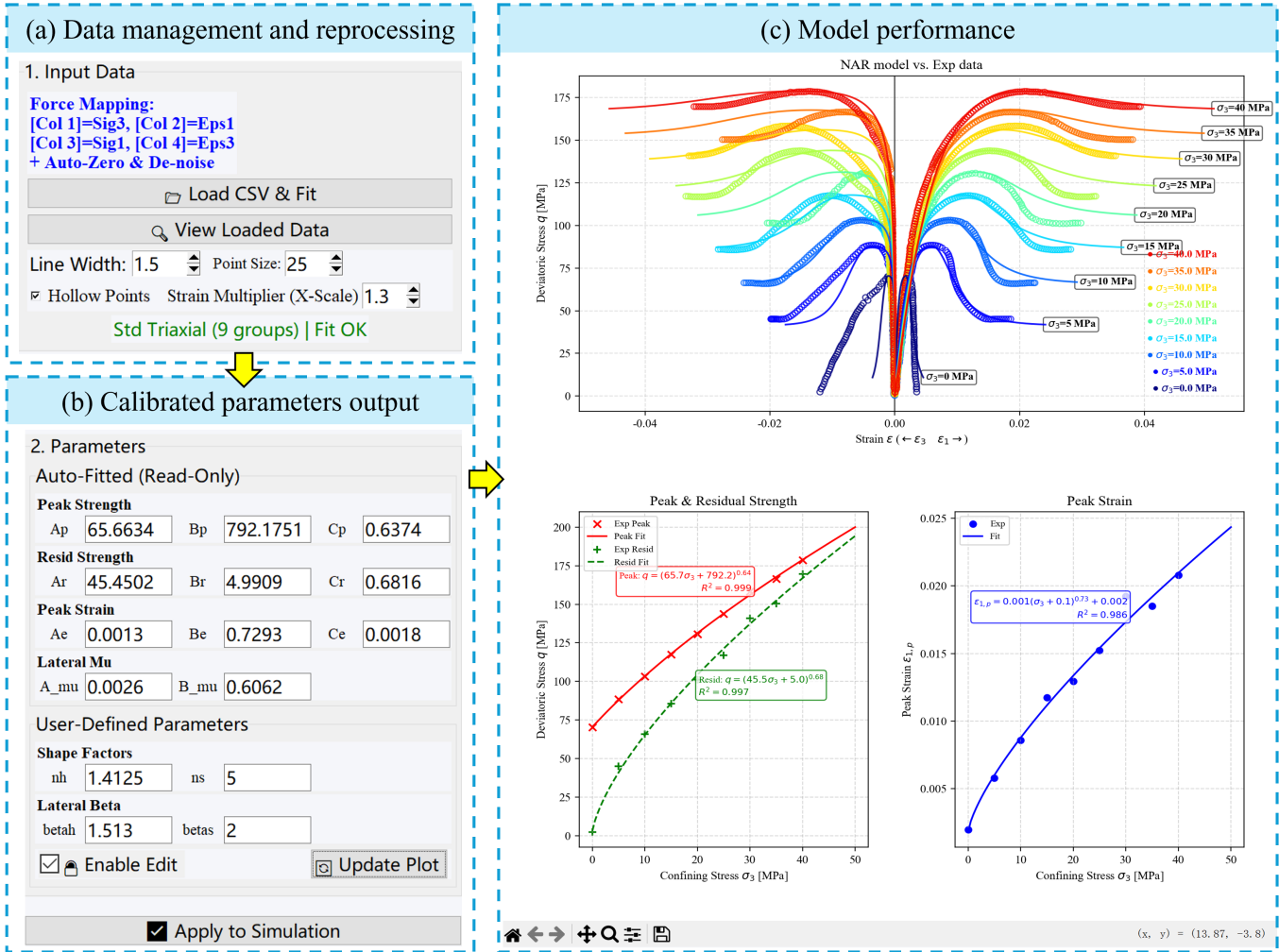
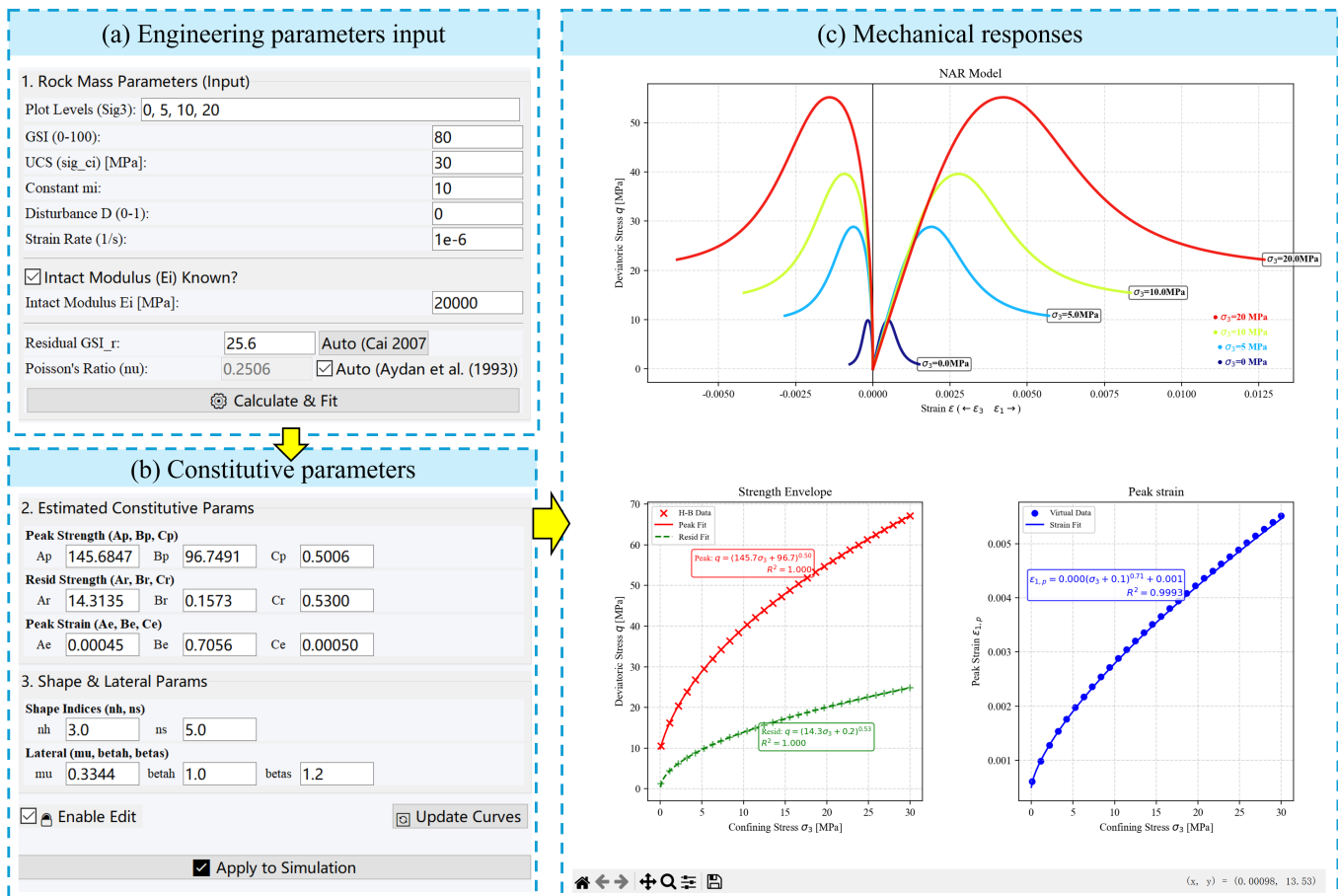


Figure 4. Operational workflow of Module 1 for experimental-data-driven calibration: (a) data management and preprocessing, (b) calibrated parameter output for quantitative inspection, and (c) visual comparison between model predictions and experimental data.

281 **Module 2: Empirical estimation for model parameters** When laboratory test data are unavailable,  
 282 Module 2 provides an empirically based workflow to transform qualitative geological indices into quantitative  
 283 constitutive model inputs, as illustrated in Fig. 5.  
 284 The process initiates with the *Engineering Input* interface (Fig. 5a), where standard descriptors ( $GSI$ ,  $\sigma_{ci}$ ,  
 285  $m_i$ ,  $D$ ) are specified. A critical feature here is the integration of strain-rate dependency; users can input a  
 286 representative strain rate to trigger the Dynamic Increase Factor (DIF) engine. The system then executes a  
 287 transformation, mapping these indices to the constitutive parameters, which are reported in the *Transformed*  
 288 *Parameter Panel* (Fig. 5b).  
 289 The reliability of the empirical estimation is finally assessed through the Mechanical Response Visualisation

(Fig. 5c), where the derived peak and residual strength envelopes are displayed. This verification step ensures that the estimated parameters consistently reflect the prescribed rock mass quality and dynamic scaling effects prior to numerical simulation.

## Calibration through empirical methods



**Figure 5. Workflow of Module 2 for empirical calibration: (a) engineering parameter input, (b) estimated constitutive parameters, and (c) mechanical response and strength envelope verification.**

## 293 Part B: Tunnel simulation kernel and interactive analysis

Upon completion of parameter determination, the workflow proceeds to Module 3, which integrates the constitutive model with a semi-analytical solution for deep tunnels through a unified interactive dashboard, as shown in Fig. 6.

The configuration interface (Fig. 6a) defines the tunnel geometry and loading conditions, including in-situ stress  $p_0$ , internal pressure  $p_u$ , tunnel radius  $R_n$ , and the number of discretised rings  $n$ . The calibrated or empirically estimated constitutive parameters are directly imported to ensure consistency with the preceding modules.

Once configured, the semi-analytical kernel computes the equilibrium mechanical response of the surrounding rock. The results are displayed in the Semi-analytical Solution Panel (Fig. 6b), which presents the radial distributions of stress and displacement, together with the stress path in principal stress space. Key response quantities, such as the strength reduction zone radius  $R_p$  and maximum displacement  $u_{\max}$ , are reported to provide immediate quantitative insight into tunnel deformation.

## Analysis of deep tunnels

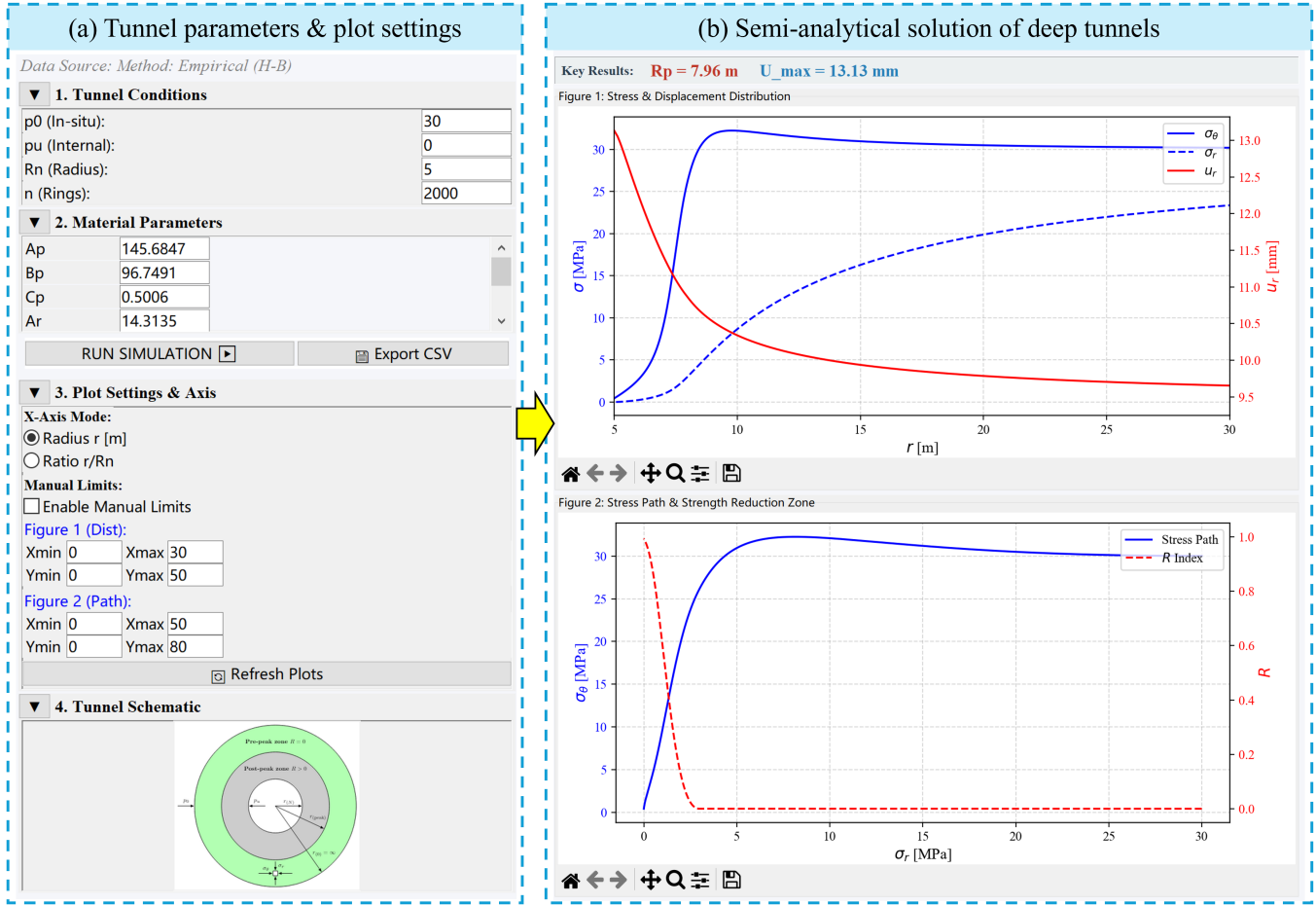


**Figure 6. Interactive dashboard of Module 3 for deep tunnel analysis: (a) definition of tunnel geometry, loading conditions, and material parameters, and (b) semi-analytical results showing stress–displacement distributions and stress path evolution.**

## 306 6. Conclusions

307 The accurate and efficient evaluation of deformation around deeply buried tunnels remains a critical problem  
 308 in deep underground engineering. In this study, a comprehensive strain-softening constitutive model incor-  
 309 porating confinement-dependent strength and post-peak dilation is implemented into a dedicated software  
 310 tool. The development of the *Tunnel Solver* GUI successfully demonstrates the practical applicability of  
 311 the theoretical framework. Automated calibration of constitutive parameters from laboratory test data is  
 312 achieved, together with a systematic procedure for estimating parameters from commonly used empirical  
 313 methods when experimental data are unavailable. The calibrated or estimated parameters are consistently  
 314 transferred to a fast semi-analytical formulation, enabling reliable and efficient prediction of tunnel deforma-  
 315 tion under deep-buried conditions. By integrating parameter determination, semi-analytical analysis, and  
 316 result visualisation within a user-friendly interface, the developed tool provides a practical solution for rapid  
 317 assessment and preliminary design in deep underground engineering, effectively bridging the gap between  
 318 constitutive modelling, semi-analytical tunnel analysis, and engineering practice.  
 319 Future work will focus on extending the framework to three-dimensional conditions by incorporating the  
 320 effect of the intermediate principal stress, as well as accounting for time-dependent deformation behaviour  
 321 such as creep.

322 **Acknowledgments**

323 Chunshun Zhang wishes to acknowledge the National Natural Science Foundation of China (No. 52278367)  
324 and the Belt and Road Special Foundation of the State Key Laboratory of Water Disaster Prevention (No.  
325 2024nkms08). Luming Shen wishes to acknowledge the financial support from the Australian Research  
326 Council through Discovery Projects Scheme (DP230100749 and DP240100851).

327 **Code and Data availability**

328 The authors highly appreciate the open-sourcing efforts and would like to make all codes involved in this  
329 research public via <https://github.com/Monash-Civil-CV-Team>. The datasets are available from the corre-  
330 sponding author on reasonable request.

331 **Conflicts of Interest**

332 The authors declare that they have no conflicts of interest.

### 333 References

- 334 Aydan, Ö., Akagi, T., & Kawamoto, T. (1993). The squeezing potential of rocks around tunnels; theory and  
335 prediction. *Rock mechanics and rock engineering*, 26(2), 137–163.
- 336 Aydan, Ö., Ulusay, R., & Kawamoto, T. (1997). Assessment of rock mass strength for underground excavations.  
337 *International Journal of Rock Mechanics and Mining Sciences*, 34(3-4), 18–e1.
- 338 Cai, M., Hou, P., Zhang, X., & Feng, X. (2021). Post-peak stress-strain curves of brittle hard rocks under  
339 axial-strain-controlled loading. *International Journal of Rock Mechanics and Mining Sciences*, 147,  
340 104921.
- 341 Cai, M., Kaiser, P., Tasaka, Y., & Minami, M. (2007). Determination of residual strength parameters of  
342 jointed rock masses using the gsi system. *International Journal of Rock Mechanics and Mining  
343 Sciences*, 44(2), 247–265.
- 344 Chen, M., Zhang, C., Canbulat, I., & Saydam, S. (2025). An enhanced empirical model for predicting  
345 continuous fracturing in rock masses. *Rock Mechanics and Rock Engineering*, 58(4), 4321–4346.
- 346 Hoek, E., Carranza-Torres, C., Corkum, B., et al. (2002). Hoek-brown failure criterion-2002 edition. *Pro-  
347 ceedings of NARMS-Tac*, 1(1), 267–273.
- 348 Hoek, E., & Diederichs, M. S. (2006). Empirical estimation of rock mass modulus. *International journal of  
349 rock mechanics and mining sciences*, 43(2), 203–215.
- 350 Honório, H. T., Houben, M., Bisdom, K., van der Linden, A., de Borst, K., Sluys, L. J., & Hajibeygi, H.  
351 (2024). A multi-step calibration strategy for reliable parameter determination of salt rock mechanics  
352 constitutive models. *International Journal of Rock Mechanics and Mining Sciences*, 183, 105922.
- 353 Hou, P., & Cai, M. (2023). A modified hoek–brown model for determining plastic-strain-dependent post-peak  
354 strength of brittle rock. *Rock Mechanics and Rock Engineering*, 56(3), 2375–2393.
- 355 Li, X., Li, L., Yan, Y., & Qi, C. (2025). A micro-macro fracture model for evaluating the brittle-ductile  
356 transition and rockburst of rock in true triaxial compression. *International Journal of Rock Mechanics  
357 and Mining Sciences*, 186, 105993.
- 358 Liu, K., Zhang, Q., & Zhao, J. (2018). Dynamic increase factors of rock strength. In *Rock dynamics and  
359 applications 3* (pp. 169–174). CRC Press.
- 360 Lu, Y., Liao, J., Wang, C., He, F., Zhang, D., Yang, Y., & Li, S. (2026). A semi-analytical solution for  
361 jamming risk in a backup system for an open tbm under high in situ stress: A case study from china.  
362 *Rock Mechanics and Rock Engineering*, 1–20.
- 363 Mao, Y., Liu, F., Li, Y., Zhao, F., He, M., & Tao, Z. (2026). Deep tunnel deformation analysis based on  
364 large-scale physical test and fractional derivative creep model. *Tunnelling and Underground Space  
365 Technology*, 170, 107383.
- 366 Meng, F., Shi, L., Hall, S., Baud, P., & Wong, T.-f. (2025). Onset of pore collapse and dilatancy in porous  
367 sandstone under true triaxial compression: Experimental observation and micromechanical modeling.  
368 *International Journal of Rock Mechanics and Mining Sciences*, 186, 105983.
- 369 Qiao, Y., Xiao, Y., Ding, W., & He, M. (2023). Effect of rock nonlinear mechanical behavior on plastic zone  
370 around deeply buried tunnel: A numerical investigation. *Computers and Geotechnics*, 161, 105532.
- 371 Shen, W. (2024). A micromechanics-based multiscale constitutive model for brittle to ductile behavior of  
372 porous geomaterial: Wq shen. *Rock Mechanics and Rock Engineering*, 57(9), 7205–7221.
- 373 Shi, M., Chen, Y., Gao, T., & Wang, Y. (2026). Accurate and reliable vision-based tunnel face rock mass clas-  
374 sification by explainable deep learning. *Tunnelling and Underground Space Technology*, 168, 107233.

- 375 Tang, Y., Wang, D., Li, J., Zhang, C., & Shen, L. (2025). A simple nonlinear constitutive model for rocks  
376 and its application to the semi-analytical solution of deeply buried tunnels. *International Journal of*  
377 *Rock Mechanics and Mining Sciences*, 195, 106255.
- 378 Wang, B., He, B.-G., Shang, J., Zhu, Z., Yu, H., & Lei, X. (2025). Failure mechanism of deep tbm tunnels  
379 subjected to dynamic disturbance under true triaxial unloading stress path. *International Journal*  
380 *of Rock Mechanics and Mining Sciences*, 191, 106128.
- 381 Wang, H., Wang, E., Song, F., Wang, W., & Rodriguez-Dono, A. (2025). Analytical solutions of non-circular  
382 deep tunnels incorporating thermal stresses: From analytical solutions to its application in shape  
383 optimization. *International Journal of Rock Mechanics and Mining Sciences*, 194, 106232.
- 384 Wang, X., Zhang, X., Li, N., Jiang, Y., Jiao, Y., & Li, B. (2025). Seismic vulnerability assessment of deep  
385 tunnels crossing multiple faults subject to earthquake forces. *Rock Mechanics and Rock Engineering*,  
386 1–20.
- 387 Xiao, Y., He, M., Qiao, Y., Peng, M., Li, H., & Cheng, T. (2023). A novel semi-analytical solution to  
388 ground reactions of deeply buried tunnels considering the nonlinear behavior of rocks. *Computers*  
389 *and Geotechnics*, 159, 105429.
- 390 Xiao, Y., Qiao, Y., He, M., Peng, M., & Zhu, C. (2024). Effect of rock nonlinear mechanical behavior on  
391 plastic zone around deeply buried tunnel: An efficient semi-analytical solution. *International Journal*  
392 *for Numerical and Analytical Methods in Geomechanics*, 48(2), 377–395.
- 393 Xing, W., Xing, H., Cai, W., Li, X., Qiu, Y., & Wang, M. (2024). Experimental study on dilatancy behavior  
394 of soft rock under dynamic loading. *International Journal of Rock Mechanics and Mining Sciences*,  
395 182, 105867.